Experimental investigation of water impact on axisymmetric bodies

G. De Backer [a,*], M. Vantorre [a], C. Beels [a], J. De Pré [a], S. Victor [a], J. De Rouck [a], C. Blommaert [b], W. Van Paepegem [b]

[a] Department of Civil Engineering, Ghent University, Technologiepark Zwijnaarde 904, B 9052 Zwijnaarde, Belgium
[b] Department of Materials Science and Engineering, Ghent University, Sint-Pietersnieuwstraat 41, B 9000 Gent, Belgium

ARTICLE INFO

ABSTRACT

The results of an elaborate experimental investigation on bottom slamming of axisymmetric objects are presented. Drop tests have been performed on a hemisphere and two conical shapes with different deadrise angles. The test setup is designed so as to prevent small rotations of the test objects which cause scatter in the measurement data. The pressure distribution and evolution as well as the body motion parameters are measured during impact. By means of a high speed camera the water uprise is visualized and the wetting factor is determined for the cones. The results are compared with a three-dimensional asymptotic theory for axisymmetric rigid bodies with constant entry velocity. The ratio between the registered peak pressures and the asymptotic theory are in accordance with comparable experiments in the literature. The asymptotic theory, however, is found to be quite conservative, since the measured peak pressure levels appear to be approximately 50% to 75% of the theoretical levels.

1. Introduction

An experimental test programme has been executed to investigate bottom slamming phenomena on point absorbers. Point absorber systems are wave energy converters consisting of oscillating bodies with horizontal dimensions that are small compared to the incident wavelength. Examples of point absorber devices are the FO³ [1] and Wave Star Energy [2]. The point absorber buoys move according to one or more degrees of freedom (heave, surge, pitch, roll) as a response to incoming waves and their kinetic energy is transferred into electrical energy either directly or by means of a hydraulic intermediate stage. Since the buoys generally have a higher natural frequency than the dominant incident wave frequencies, the point absorber response is often tuned to the characteristics of the incoming wave spectrum by increasing the system inertia or by applying latching control [3]. This enables the point absorber to operate closer to resonance conditions, which increases the energy capture. However, it might cause the buoys to rise out of the water which results in slamming back into the water surface on re-entry. This phenomenon occurs particularly for point absorbers with a small draft in an energetic wave climate. Slamming can be reduced by influencing the control parameters of the buoy, i.e. by increasing the damping and/or by detuning the buoy. However, these measures result in power absorption losses as shown in [4,5]. Consequently, a certain level of slamming will usually be allowed. For this reason it is important to know to which pressure magnitudes the body is exposed when slamming occurs. This paper aims to investigate bottom slamming on point absorbers by means of experimental drop tests. The results are compared with analytical results obtained by Chuang [6] and Faltinsen and Zhao [7].

Slamming phenomena have been studied over several decades especially in naval hydrodynamics. Pioneering research has been carried out by von Karman [8] and Wagner [9]. Wagner studied the water impact on rigid two-dimensional bodies by approximating the bodies with a flat plate and taking into account the water uprise on the body in a simplified way. Because of the blunt body approach, the bodies are assumed to have small deadrise angles in the range of 4 up to 20 degrees [10]. Zhao and Faltinsen presented numerical results, based on the findings of Dobrovol'skaya [11], for two-dimensional bodies with deadrise angles between 4 and 81 degrees [12,13]. Inspired by Zhao's work, Mei et al. [14] developed an analytical solution for the water impact problem of general two-dimensional bodies. The main difference with the Wagner method is that the exact body boundary conditions are fulfilled, instead of approximating the body by a flat plate. The advantage of Wagner's approximation is the ability to use analytical expressions for the velocity potential. However, with the generalized Wagner method, a broader range of (local) deadrise angles can be investigated in a more accurate way.

---

* Corresponding author. Tel.: +32 9 264 54 93; fax: +32 9 264 58 37.
 E-mail address: griet.debacker@ugent.be (G. De Backer).

Nomenclature

b_0	wet radius at the undisturbed free water surface [m]
b	wet radius at the immediate free water surface [m]
C_p	slamming pressure coefficient [-]
C_v	coefficient of variation [-]
C_w	wetting factor [-]
F	force [N]
g	gravitational acceleration [m/s^2]
h	drop height [m]
h^*	equivalent drop height corresponding to the measured impact velocity [m]
l_{jet}	jet height [m]
M	body mass [kg]
$M_{a_{33}}$	infinite frequency limit of the added mass [kg]
p	pressure [bar $= 10^5$ Pa]
r	radial coordinate [m]
R	radius of hemisphere [m]
$R*$	Pearson correlation coefficient [-]
t	time [s]
U	entry velocity [m/s]
z	vertical coordinate [m]
β	deadrise angle [deg][rad]
ζ	water elevation at intersection with body [m]
ρ	mass density of fluid [kg/m^3]

A substantial amount of experimental work has been performed to validate the analytical and numerical models. Lin and Shieh [15] experimentally investigated the pressure characteristics of a cylinder during water impact. They also visualized the flow pattern during penetration by making use of a digital imaging system and a high speed data acquisition system. Zhao and Faltinsen [13] performed drop tests to study two-dimensional flow situations of horizontal wedges dropped onto the free water surface. Experiments by Yettou [16] et al. consist of free fall drop tests on symmetrical wedges. They investigated the influence of the drop height, the deadrise angle and the mass of the wedge and compared the results with existing models from Mei et al. [14] and Zhao and Faltinsen [13].

Most studies have focused on two-dimensional impact problems since slamming on ships has been a major concern. However, there is a need for three-dimensional solutions because real impact phenomena are three dimensional. In this paper, vertical slamming of three-dimensional objects, more specific axisymmetric bodies, is considered. Early studies in this area have been published by Shiffman and Spencer [17,18]. They investigated vertical slamming phenomena on spheres and cones analytically by approximating the bodies as a lens and an ellipsoid and presented solutions for the impact force on these axisymmetric objects. Wagner's theory has been extended to axisymmetric bodies by Chuang [6] and Faltinsen and Zhao [7]. In the case of axisymmetric objects, the body shape is approximated with a growing flat disc analogous to Wagner's flat plate approximation for two-dimensional shapes. Based on this principle, Chuang [6] developed an analytical expression for the pressure distribution on a cone with small deadrise angle. In 1997 Faltinsen and Zhao [7] presented an asymptotic theory for water entry of hemispheres and cones with small (local) deadrise angles based on the assumptions behind the Wagner theory. Another important contributor to axisymmetric slamming problems is Miloh [19–21] who developed analytical expressions for the slamming forces on axisymmetric bodies. One of the main differences between his work and Wagner's theory is that the body boundary conditions are satisfied exactly on the actual body surface instead of on a flat disc.

In 2003 Battistin and Iafrati [22] numerically studied impact loads and pressure distributions on two-dimensional and axisymmetric bodies. Two years later Faltinsen and Chezhian [23] presented a generalized Wagner method for three-dimensional slamming based on the approach presented by Zhao et al. [13] for two-dimensional water impact problems. To validate the numerical simulations, they performed drop tests on a three-dimensional shiplike composite structure from which they obtained several force measurements. Peseux, Gornet and Donguy [24] solved the three-dimensional Wagner problem numerically for both rigid and deformable bodies. The numerical model is validated with an interesting experimental investigation consisting of drop tests of conical shapes with small deadrise angles ($6° - 10° - 14°$). Kim and Hong [25] numerically studied the impact of arbitrary three-dimensional bodies with an extended von Karman and an extended Wagner approach, including the presence of incoming waves. They also presented experimental results on the impact loads during water entry of three-dimensional structures.

Very few experiments are available for validation of theoretical pressure predictions for axisymmetric bodies. In 1961 Nisewanger [26] performed drop tests on aluminium hemispheres and measured pressure distributions with self-made pressure transducers. For conical shapes, experimental research has been carried out by Chuang and Milne [27] in 1971 and more recently by Peseux et al. as mentioned above. In the former study impact pressures are measured on cone shapes with small deadrise angles varying from 1° to 15°. Point absorbers with a conical shape are very likely to have larger deadrise angles ($\geq 20°$). In this paper the results of new impact experiments on a hemisphere and on cone shapes with larger deadrise angles are presented.

2. Experimental design

2.1. Test setup and test objects

Table 1 shows the three different bodies that have been tested: a hemisphere and two cones with deadrise angles of 20° and 45°. The models are made from polyurethane and have a large thickness from 30 mm to 50 mm. As mentioned in Table 1 the diameter of the objects is 0.30 m, which is sufficient to reduce surface tension effects. The bodies are dropped in a water basin with horizontal dimensions of 1.20 m by 1.00 m and a height of 1.25 m. Twelve different drop heights between 0.05 m and 2.00 m have been evaluated, corresponding to impact velocities of 1.0 m/s and 6.3 m/s. A realistic stroke for a point absorber buoy is about 5 to 10 m. Dependent on the control parameters, a free fall of 2 m can be considered as an extreme case. Smaller drop heights will occur more frequently and are therefore relevant as well. Because of reasons of similitude, the cone shape tests can be considered as full-scale tests, apart from the fact that the masses are not correctly scaled. In case of the hemisphere, the results from the smallest drop heights (0.05 m–0.20 m) need to be upscaled to prototype values, according to the dimensions of a full-scale body. Expected scaling effects might arise from surface tension and viscous effects. For completeness, the tests with the hemisphere are also performed for larger drop heights.

In this paper, the results of an improved test setup are presented. Initially the tests were carried out without any guiding structure. Although the test objects were balanced precisely, the scatter in the measured data appeared to be significant. In order to prevent small rotations of the floaters while falling down, the setup was equipped with a guiding system consisting of tightened steel wires [5]. The results discussed in this paper, however, are obtained from a test setup with an improved guiding system. The tightened steel rods are replaced by a rail mounted on stiff aluminium profiles. The test bodies are attached to a profile structure equipped
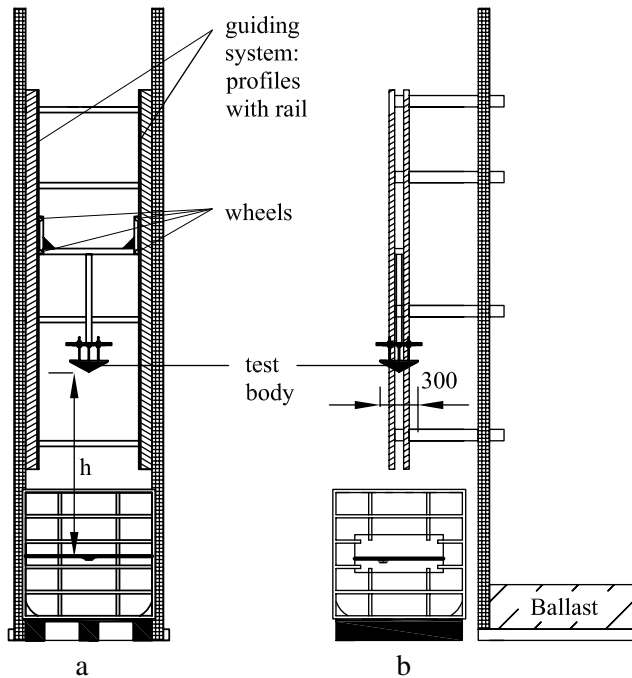
Fig. 1. Schematic view of the experimental test setup [mm].

Fig. 2. Picture of the experimental test setup.

with wheels, rolling down the rail as shown in Fig. 1. With this test setup the verticality of the impacting object is assured and the tests are very well reproducible. The masses mentioned in Table 1 correspond to the total falling mass, i.e. the sum of the mass of the polyurethane bodies and the aluminium carriage. The drop height, h, is limited to 2 m, compared to 4 m for the original test setup. A 10 mm plexiglass sheet is installed in the basin which allows to film the impact phenomena. A picture of the test setup is given in Fig. 2.

Table 1
Test object characteristics.

Test objects (dimensions in mm)	Characteristics
	Hemisphere Local deadrise angles: 7.7° and 18.4° Radius: 0.15 m Material thickness: 0.05 m Mass: 11.5 kg
	Cone Deadrise angle: 20° Max. radius: 0.15 m Material thickness: 0.03 m Mass: 9.8 kg
	Cone Deadrise angle: 45° Max. radius: 0.15 m Material thickness: 0.03 m Mass: 10.2 kg

Table 2
Sensor characteristics.

| Sensor	Measurement range	Resonance frequency (kHz)
A07	3.45 bar	≥ 250
K30, K31	2 bar	≥ 150
Shock accelerometer	500 g	≥ 54

2.2. Instrumentation

#### 2.2.1. Pressure sensors and shock accelerometer

The pressure time history, the position and deceleration of the body were recorded during impact. Three high frequency piezoelectric pressure sensors were used. One ICP pressure sensor (A07) has a built-in microelectronic amplifier while two other high frequency pressure sensors (K30, K31) have external amplifiers. The measurement range for these devices is 3.45 bar and 2 bar, respectively. The pressure cells have a small diaphragm of 5.5 mm and a very high resonance frequency, see Table 2. Consequently the sensors are very well suited for measuring impact phenomena. The sensors are flush-mounted at a horizontal distance of 0.04 m and 0.09 m, respectively from the symmetry axis, as illustrated in Table 1. The deceleration of the object during impact was measured by a shock accelerometer with a measurement range up to 500 g and a resonance frequency of 54 kHz.

Fig. 3 shows the configuration of the pressure cells. The first three configurations (a–c) represent the sensor positions for the hemisphere. The sensors in Fig. 3(a) are mounted on two opposite meridians in order to evaluate the verticality of the penetration. With the configuration in Fig. 3(b) a comparison between the two local deadrise angles can be made and in Fig. 3(c) the sampling frequency is increased up to 100 kHz for one pressure sensor and the shock accelerometer. In Fig. 3(d) and (e) the configuration of the pressure sensors is given for the 20° cone. In each configuration two different pressure sensors are mounted on meridians close to each other, allowing for the assessment of the different sensors. Fig. 3(f) shows the pressure sensor configuration in case of the 45° cone, which is similar to Fig. 3(a) combined with (b). Each case has been tested at least three times for every drop height, varying between 0.05 m and 2 m.

A sampling frequency (SF) of at least 30 kHz was used for recording. Such high sampling frequencies are required, since the
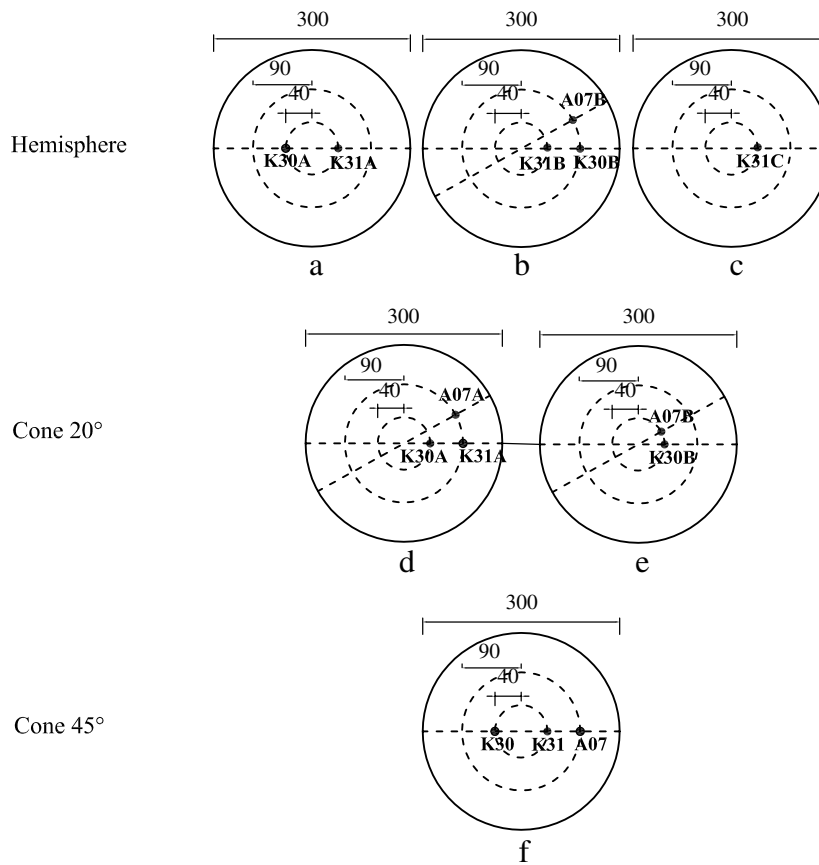
Fig. 3. Pressure sensor positions [mm] for the hemisphere: (a) Sensors K30A and K31A - SF = 30 kHz, (b) Sensors K30B, K31B and A07B - SF = 30 kHz, (c) Sensor K31C - SF = 100 kHz, for the 20° cone : (d) Sensors K30A, K31A and A07A - SF = 30 kHz, (e) Sensors K30B and A07B - SF = 30 kHz, for the 45° cone: (f) Sensors K30, K31 and A07 - SF = 30 kHz.
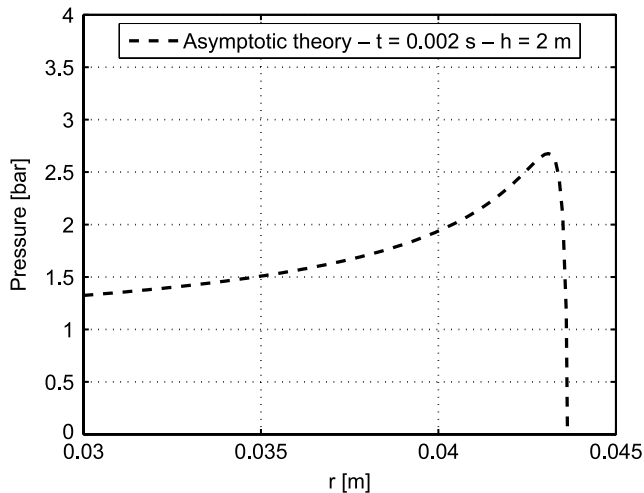
Fig. 4. Theoretical pressure distribution as a function of r for a cone with deadrise angle 20° and drop height 2 m.

pressure peaks occur in a very small time interval (order of magnitude milliseconds). For the same reason the resonance frequency of the sensors should be high enough. A small pressure cell diaphragm area is necessary since the pressure peaks are also very much localized in space as well, as can be seen in Fig. 4, showing the theoretically predicted pressure distribution according to asymptotic theory at $t = 0.002$ s for a cone with deadrise angle 20° and drop height 2 m.

Table 3
Influence of pressure sensor diameter: estimated deviations from peak pressure for drop heights of 1 m and 4 m.

Sensor diameter (mm)	$h = 1$ m (%)	$h = 4$ m (%)
5.5	10.8	13.9
19	30.5	34.2

In earlier investigations, sensors with larger diameters have sometimes been used, with values up to 19 mm in [16]. In that case the pressure peaks might have a smaller spatial extent than the sensor area. Even pressure cells with diameter 5.5 mm might measure a space-averaged pressure, which is slightly different from the peak pressure. The pressure distribution is particularly more peaked when the (local) deadrise angle is small and the impact velocity high. Assuming that a pressure cell registers the space-averaged pressure when subject to a non-uniform pressure distribution, the deviation between the peak pressure and the sensor record can be determined. In [23], Faltinsen estimated that the theoretical peak pressure is at maximum 11% higher than the space-averaged pressure, measured by a sensor with a diameter of 4 mm. Deviations of the same magnitude can be derived, based on the theoretically predicted pressure distribution by the three-dimensional asymptotic theory. For pressure cells with diameter 5.5 mm it is estimated with the latter method that the measured pressure on a cone with deadrise angle 20° deviates between 10% and 14% from the peak pressure for drop heights of 1 m and 4 m. In a similar way as above, it is expected that a pressure sensor with a diameter of 19 mm, would underestimate the peak pressure with more than 30% for the same case of a cone with deadrise angle 20°, as shown in Table 3.

2.2.2. High speed camera

A high speed camera was used to record the penetration of the impacting bodies as a function of time. The camera provided information on the water uprise along the body and on the position and velocity of the impacting body. For this purpose a marker tracking technique has been applied. The high speed camera is able to deliver images up to 250 000 frames per second (fps) and has full mega pixel resolution at 3000 fps. In this test case, it has been used at 5000 up to 18 000 fps, dependent on the desired pixel resolution. Because of the high frame rate, the camera shutter time is extremely short. In order to overcome low illumination and to avoid interference with the grid frequency, special flicker free lights have been used. Two lasers are mounted on top of the basin and serve as a trigger for the data acquisition system. When the dropped objects intersect the laser beams, the recording of the pressure sensors, accelerometer and camera signal starts automatically.

3. Analytical formulation

The experimental results are compared with existing asymptotic solutions based on the classical Wagner method extended to axisymmetric bodies, as it was proposed by Chuang [6] and Faltinsen et al. [7]. Despite the interesting work that has already been carried out in the field of water impact, Wagner's method is even nowadays still very valuable, since it produces analytical formulas that are easy to handle and give a very good first insight into the problem. The fluid flow is described by potential theory and a constant entry velocity U is assumed. The initial time instant t_0 is defined as the time where the body touches the calm water surface. At a time t, the penetration depth relative to the calm water surface ($z = 0$) equals Ut and the corresponding instantaneous radius at the wet section of the cone is $b_0(t)$, as shown in Fig. 5. The instantaneous radius $b(t)$ at the intersection point between the body and the water is found by integrating the vertical velocity of the water particles at $z = 0$. For a cone shape this results in $b(t) = 4Ut/(\pi \tan \beta)$ [7]. It should be mentioned that Fig. 5 gives a simplified presentation of the water uprise, since in reality a jet flow occurs which might end in a spray, depending on the convexity of the object.

The pressure on a cone shape with deadrise angle β, at a certain distance r from the symmetry axis, is expressed by:

$$p_{cone} = \frac{1}{2}\rho U^2 \left[1 - \frac{4\left(\frac{r}{Ut}\right)^2}{\pi^2 \left(\frac{16}{\pi^2 \tan^2 \beta} - \left(\frac{r}{Ut}\right)^2\right)} \right.$$
$$\left. + \frac{64}{\pi^3 \tan^2 \beta \sqrt{\frac{16}{\pi^2 \tan^2 \beta} - \left(\frac{r}{Ut}\right)^2}} \right]. \tag{1}$$

Eq. (1) is composed of three terms. The first term expresses the stagnation pressure. The second term is a consequence of the permanent flow around the disc and the third term accounts for the expansion of the disc, representing the effect of the non-stationary behaviour of the flow around the disc. As mentioned before, the blunt body assumption in Wagner's method implies that bodies should have small local deadrise angles. In the literature, it is stated that the classical Wagner theory gives quite accurate results for wedges with deadrise angles in the range of 4 to 20 degrees [13]. When deadrise angles are smaller than 4 degrees, an air cushion is formed, which reduces the pressure on the structure and as a result, Wagner theory overestimates the pressure by a large margin.

For a hemisphere the relationship between the penetration depth and instant wet radius b is not as straightforward as it is for a cone shape. Faltinsen and Zhao [7] suggested a quadratic relation between Ut and b which is only valid for small submergences
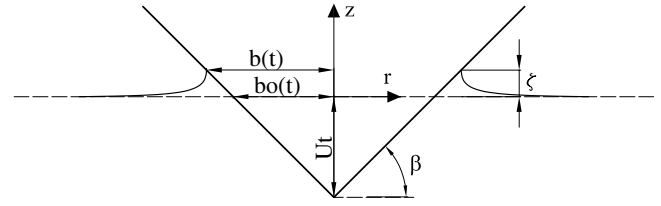

Fig. 5. Cone penetrating through originally calm water: clarification of parameters.

($Ut/R < 1/5$) : $b = \sqrt{3RUt}$. The pressure on an impacting hemisphere with radius R, at a distance r from the symmetry axis, is expressed as follows:

$$p_{hemisphere} = \frac{1}{2}\rho U^2 \left[1 - \frac{4\left(\frac{r}{Ut}\right)^2}{\pi^2 \left(\frac{3R}{Ut} - \left(\frac{r}{Ut}\right)^2\right)} + \frac{6}{\pi \sqrt{\frac{3Ut}{R} - \left(\frac{r}{R}\right)^2}} \right]. \tag{2}$$

The measured penetration and acceleration will be compared with theoretical values that are based on the computation of the hydrodynamic impact force, F_3, acting on a body penetrating the free water surface. This force is calculated in two ways. By making use of the added mass theorem (AM), F_3 can be expressed as:

$$F_3 = \frac{d\left(M_{a_{33}}U\right)}{dt} = M_{a_{33}}\frac{d^2z}{dt^2} + \frac{dM_{a_{33}}}{dt}\frac{dz}{dt} \tag{3}$$

where $M_{a_{33}}$ is the high frequency limit of the added mass. The second term in Eq. (3) can also be computed by integration of the pressures given in Eqs. (1) and (2). This will be referred to as the pressure integration (PI) method. When F_3 is known, the acceleration at each time step is derived and the velocity and penetration depth are obtained by numerical integration of the acceleration.

4. Experimental test results

4.1. Water uprise and impact velocity

Fig. 6 shows a selected number of images of a hemisphere penetrating the free water surface, dropped from 1 m. A software program recognizes the pattern of the marker and determines its coordinates at each time step. Consequently the position of the body is known as a function of time and the velocity can be determined. The pictures clearly show the water uprise along the hemisphere. The jet flow is quickly detached from the body surface ending up in a spray. This phenomenon has also been observed for cylinders by Greenhow and Lin in [28] and [29]. Figs. 7 and 8 show camera images of the impacting cones for a drop height of 1 m. The creation and propagation of a jet along the cone surface can be clearly seen and measured.

From the photographs of the cones the ratio C_w can be determined and compared with theoretical values. The C_w factor is defined as the ratio between the heights of the immediate and undisturbed free water surfaces measured from the bottom point of the falling object:

$$C_w = 1 + \frac{\zeta(b, t)}{Ut} \tag{4}$$

with ζ the z-coordinate of the intersection point between the object and the free water surface, see Fig. 5. When flow separation occurs above ζ, as in the case of the hemisphere, C_w has the physical meaning of a wetting factor. However, in the case of a cone a thin jet flow might occur above this intersection point as observed in Figs. 7 and 8. The wetting factor C_w for a cone with attached jet flow can then be defined as:

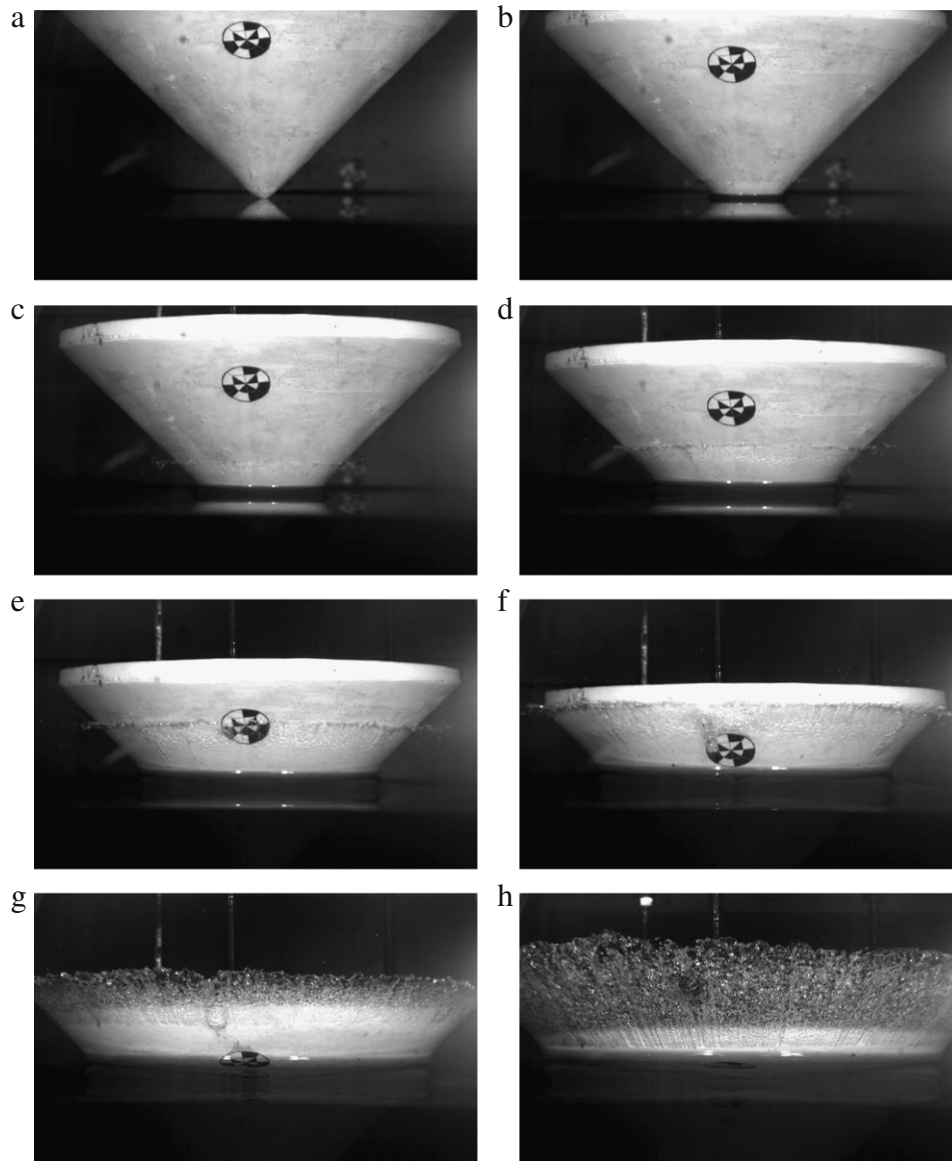$$C_w = 1 + \frac{\zeta(b, t) + l_{jet}}{Ut} = \frac{b}{b_0} + \frac{l_{jet}}{Ut} \tag{5}$$

where l_{jet} is the height of the jet. Considering the outer flow
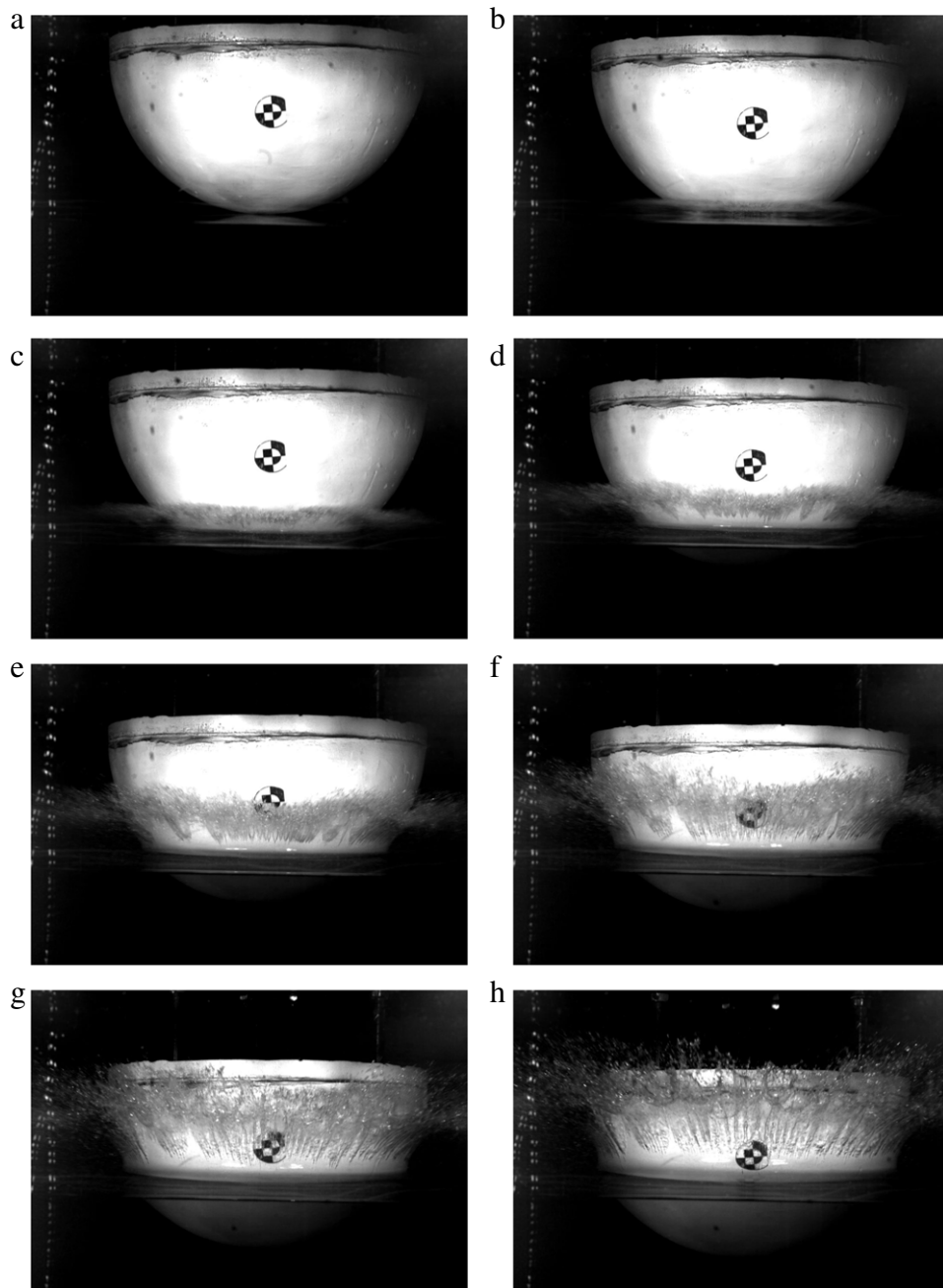
Fig. 6. Hemisphere penetrating the water – (a) $t = 0.0000$ s, (b) $t = 0.0022$ s, (c) $t = 0.0044$ s, (d) $t = 0.0066$ s, (e) $t = 0.0088$ s, (f) $t = 0.0110$ s, (g) $t = 0.0132$ s.
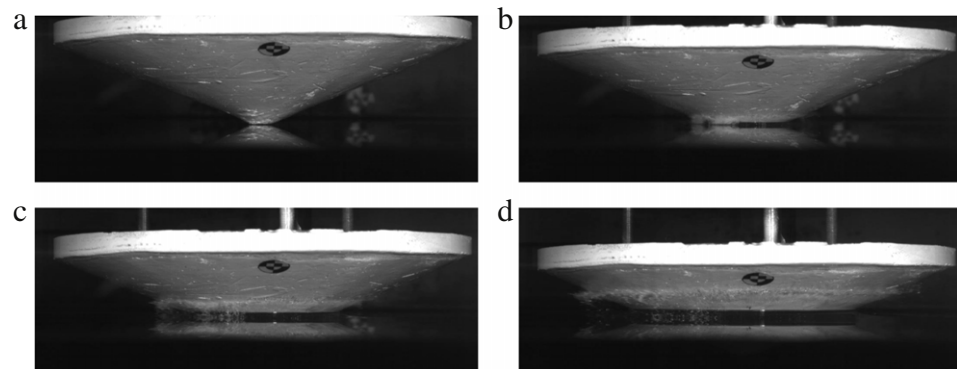
Fig. 7. Cone ($\beta = 20°$) penetrating the water – (a) $t = 0.0000$ s, (b) $t = 0.0044$ s, (c) $t = 0.0088$ s, (d) $t = 0.0132$ s.

Fig. 8. Cone ($\beta = 45°$) penetrating the water – (a) $t = 0.000$ s, (b) $t = 0.004$ s, (c) $t = 0.008$ s, (d) $t = 0.012$ s, (e) $t = 0.016$ s, (f) $t = 0.020$ s, (g) $t = 0.024$ s, (h) $t = 0.028$ s.

domain, Faltinsen et al. [7] found a ratio b/b_0 equal to $4/\pi$ for cones based on Wagner's blunt body approach. By matching the outer three-dimensional solution for axisymmetric flow with the inner two-dimensional jet flow solution by Wagner, Faltinsen described the jet flow during water entry of a cone. Based on Faltinsen's considerations, the height of the jet is found to be $\frac{4Ut}{\pi}\cos\beta$, resulting in a wetting factor C_w equal to $\frac{4}{\pi}(1+\cos\beta)$ for a cone with attached jet flow. The formula by Faltinsen et al. [7] is slightly different from the latter, probably due to a typing error in [7]. In numerical models that satisfy the real body boundary conditions, the description of the jet flow can be very complex. Zhao and Faltinsen [12] developed a numerical model that significantly simplifies the description of the jet flow. This approach has been adopted by Battistin and Iafrati [22] who determined the water surface elevation numerically for axisymmetric bodies, among them a cone with deadrise angle 30°. However, the jets are truncated at the top, which makes it impossible to derive the correct wetting factor. Figs. 9 and 10 illustrate the wetting factor as a function of penetration depth for three different drop heights for the 45° cone and

the 20° cone, respectively. The value of C_w is relatively constant during penetration, although in both cases slightly higher values are measured for small penetration depths. Furthermore the influence of the drop height appears to be not very significant and a smaller wetting factor is found for the highest deadrise angle. On average the measured values are 19% and 23% smaller than the values found by Faltinsen et al. for the 45° and 20° cone, respectively. For the hemisphere it is not possible to derive the wetting factor by means of the camera images, since it is difficult to correctly determine the intersection point between the free water surface and the body, due to the disturbing effect of the three-dimensional spray. In order to better visualize the flow separation at the hemisphere, it would be necessary to create a light sheet through the symmetry axis of the hemisphere by means of a strong laser. In that case the water spray particles in front of the hemisphere are not illuminated and do not disturb the measurement.

Fig. 11 illustrates the velocity during the initial impact stage determined by the high speed camera as a function of the entry depth. For each shape three initial velocities, U_0, are considered:
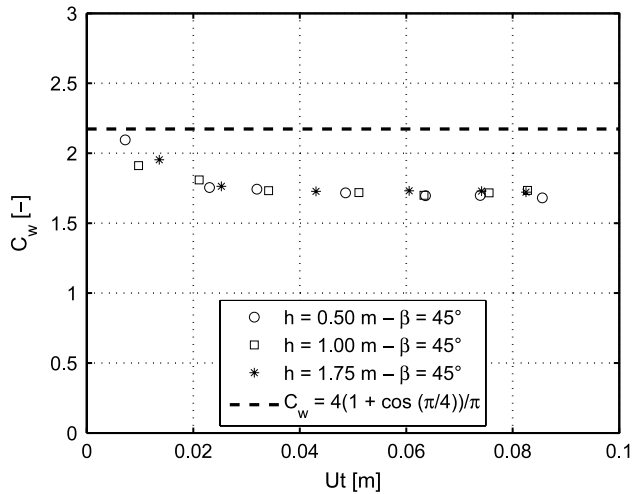
Fig. 9. Wetting factor as a function of penetration depth on the 45° cone.

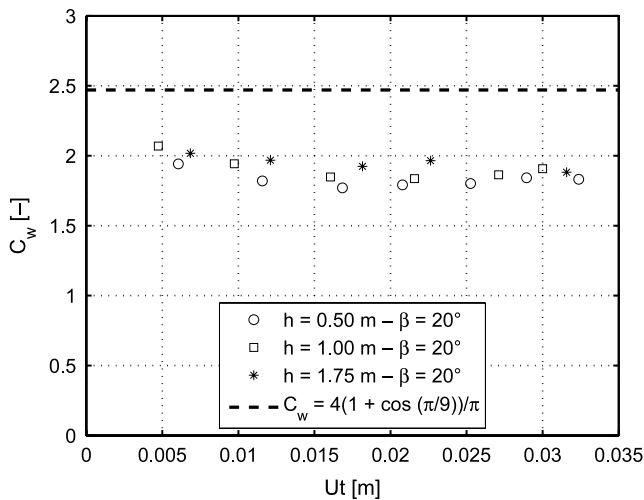**Fig. 10.** Wetting factor as a function of penetration depth on the 20° cone.

$U_0 < 3$ m/s, $U_0 \approx 4$ m/s and $U_0 > 4.6$ m/s. Although the mass of the hemisphere is the largest of the three tested objects, the velocity decrease during the initial stage of the impact is most pronounced for this shape. This is especially the case for higher drop heights, corresponding to larger values of U_0 and consequently higher impact forces.

For the 45° cone the slamming force is so small that the impact velocity remains quite constant. Note that the velocity increases for both cone shapes in particular for small values of U_0. Immediately after contacting the water surface, the impact forces on the cones are still rather small compared to the gravity force. For this reason the impact velocity first builds up for a very short period of time before starting to decrease. The graph illustrates that the assumption of a constant entry velocity can be better justified for smaller initial velocities U_0. The recorded velocity time history is short for the 20° cone, because the marker pattern becomes quickly unclear due to the water uprise. Longer velocity time histories are obtained with the accelerometer, as will be illustrated in Section 4.2.

4.2. Pressure distribution, impact velocity and deceleration

4.2.1. Hemisphere

Figs. 12 and 13 show the pressure coefficient $C_p = p/(0.5\rho U_0^2)$ on the hemisphere as a function of time for a drop height of 1 m at
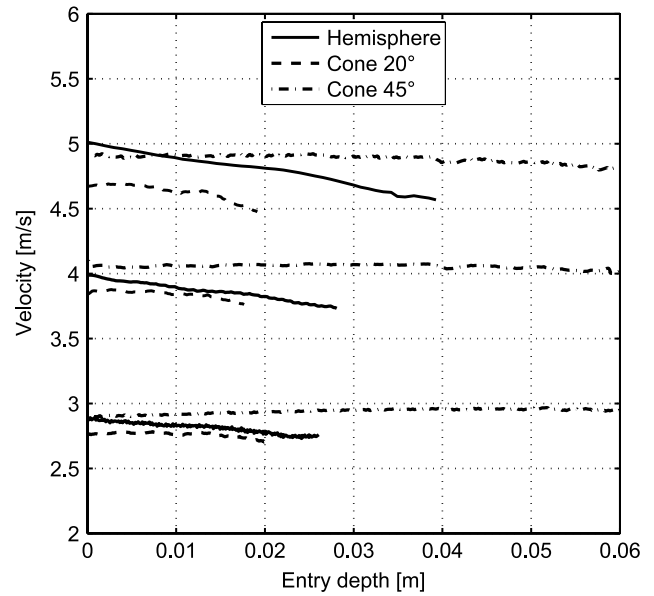
Fig. 11. Velocity measured by the high speed camera for three different initial impact velocities for each shape.

$r = 0.04$ m and $r = 0.09$ m, respectively. The initial time is defined as the moment where the bottom of the hemisphere touches the water surface. The pressure measurements are compared with the asymptotic solutions, assuming a constant entry velocity. The figure indicates that the asymptotic theory overestimates the pressures significantly, particularly for small local deadrise angles. This was also observed in the experiments of Lin and Shieh [15] for a cylinder. The pressure profiles indicate that smaller local deadrise angles lead to higher pressures which have a shorter duration in time. The rising time of the first pressure peak (Fig. 12) is only 0.2 ms. Due to the decrease in velocity, the time interval between the measured pressure peaks is larger than between the theoretically predicted peaks. Furthermore it can be noted that the pressure distribution of the four sensors at $r = 0.04$ m obtained from the three different test configurations in Fig. 3 (a–c) coincide very well. This implies firstly that the hemisphere penetrated perfectly along a vertical line and secondly that a sampling frequency of 30 kHz is sufficiently large since no higher peak has been registered at 100 kHz.

Figs. 14–16 show the measured and theoretical acceleration, velocity and entry depth, respectively. The theoretical values are based on the pressure integration method (PI) and added mass method (AM) as explained in Section 3. The presented velocity and position data from the high speed camera are measured at 18000 fps for the three shapes. The acceleration signal in Fig. 14 is disturbed by a high frequency noise, probably originating from oscillations of the horizontal aluminium beam since the noise was not registered in the original setup. Nevertheless the accelerometer signal is still valuable, as can be seen in Fig. 15. The velocity, based on numerical integration of the accelerometer signal coincides very well with the velocity derived from the high speed camera images. The theoretical velocities drop more quickly, which is due to the fact that the forces and consequently the accelerations are overestimated by both methods. The measured initial velocity is 4.0 m/s, whereas the calculated speed $U_0 = \sqrt{2gh}$ would be 4.4 m/s. This difference can be attributed mainly to friction in the guiding system. For this reason all theoretical values are calculated based on the measured initial speed. Note the very short time span of 12 ms in the plots. In this time span the hemisphere has reached a submergence of about $R/3$ (see Fig. 16) and the relevant impact phenomena have occurred.
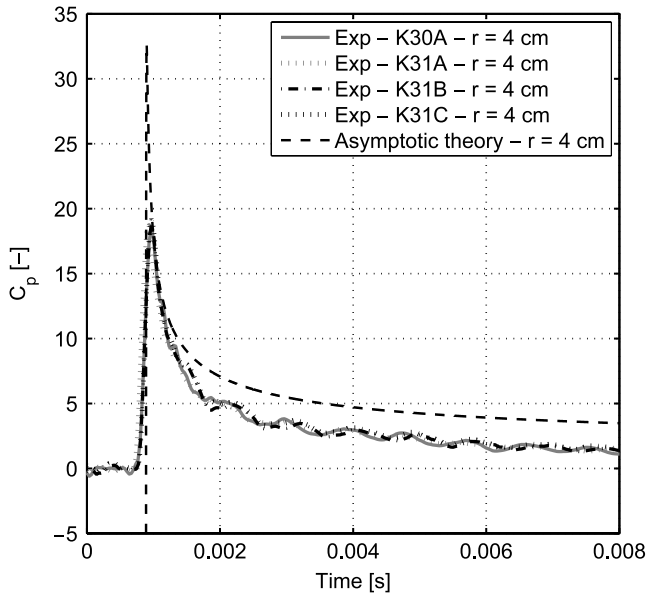
Fig. 12. Measured and calculated pressure distribution on the hemisphere at $r = 0.04$ m for $U_0 = 4.0$ m/s.
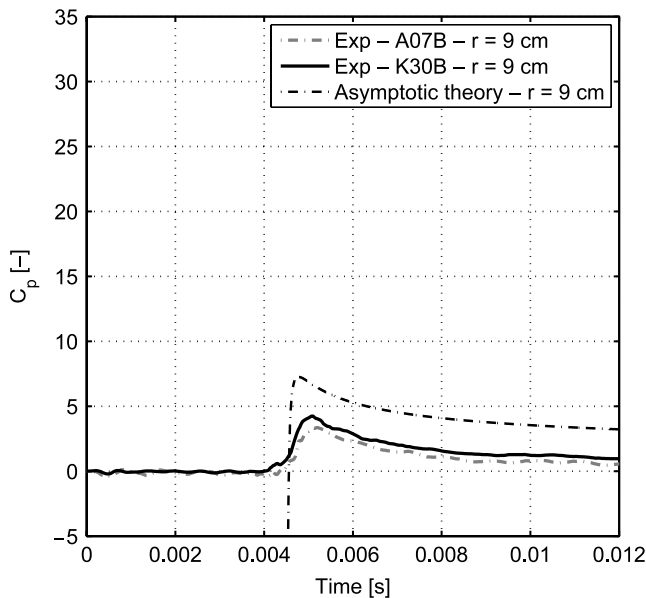

Fig. 13. Measured and calculated pressure distribution on the hemisphere at $r = 0.09$ m for $U_0 = 4.0$ m/s.

4.2.2. Cone 20°

Fig. 17 shows the measured and calculated pressure distribution on the 20° cone for a measured impact velocity $U_0 = 3.85$ m/s. It can be noticed that the pressures measured with the different sensor types correspond very well in both sensor positions $r = 0.04$ m and $r = 0.09$ m. According to the asymptotic theory, the peak pressure level does not change along the object. In the experiments the second pressure peak is slightly larger than the first one. On average over all the tests, the difference in peak pressure between the two positions is 3.8%. This phenomenon was also observed by Peseux et al. [24] with even more pronounced differences for cones with smaller deadrise angles ($14° - 10° - 6°$). The reason for this trend is not entirely clear. It could possibly be attributed to mounting problems due to the small radius of curvature at $r = 0.04$ m compared to $r = 0.09$ m. The sensors, having a flat membrane area, disturb the geometry of the cone more at
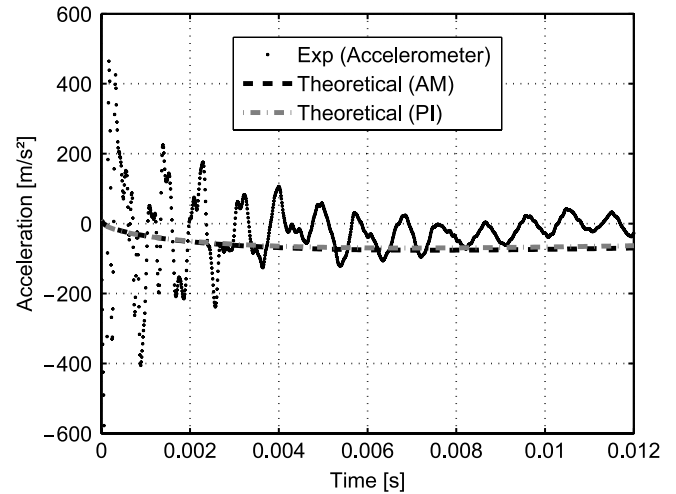
Fig. 14. Measured and calculated acceleration on the hemisphere.
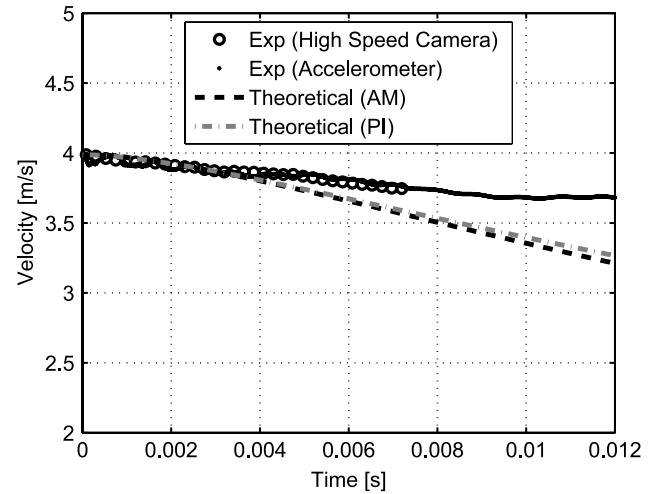
Fig. 15. Measured and calculated velocity on the hemisphere.
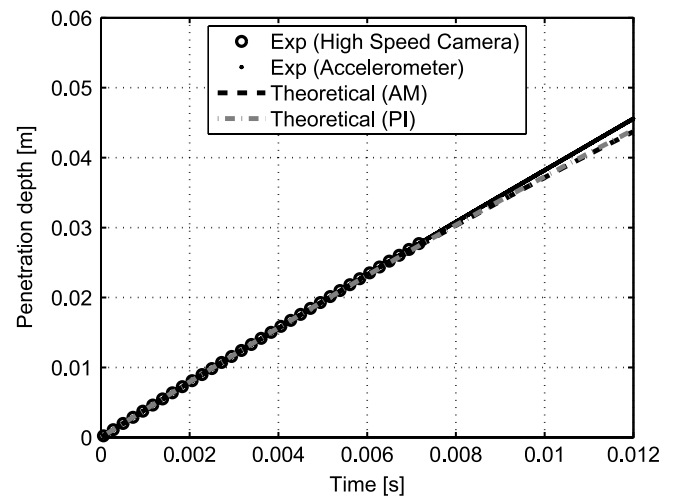

Fig. 16. Measured and calculated position on the hemisphere.

a smaller radius of curvature and this might slightly influence the pressure measurement.

In Fig. 18 a quite high deceleration peak of about -100 m/s^2 can be noticed, which results in a non-negligible velocity decrease (Fig. 19). As in the case of the hemisphere, the theory is rather
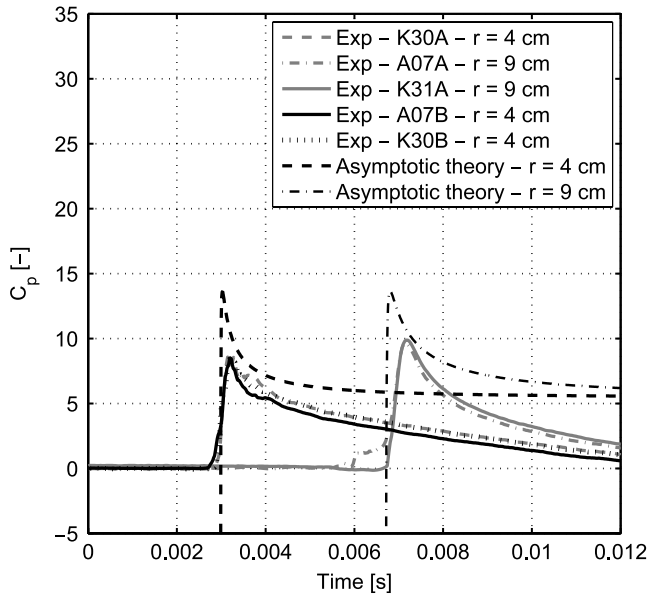
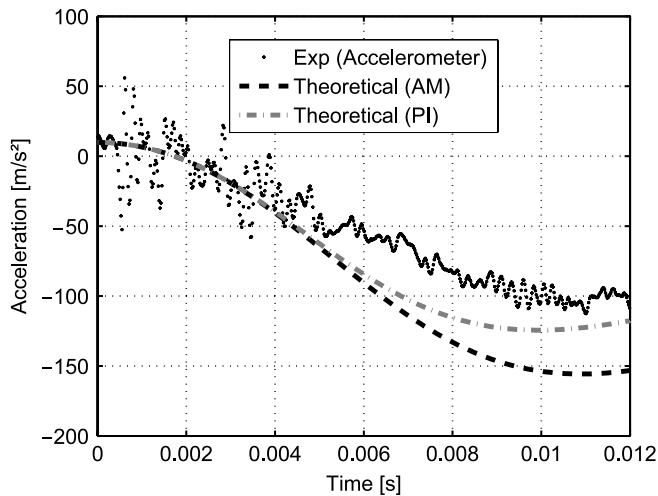**Fig. 17.** Measured and calculated pressure distribution on cone ($\beta = 20°$) for $V_0 = 3.85$ m/s.

Fig. 18. Measured and calculated acceleration on cone ($\beta = 20°$).

Fig. 19. Measured and calculated velocity on cone ($\beta = 20°$).
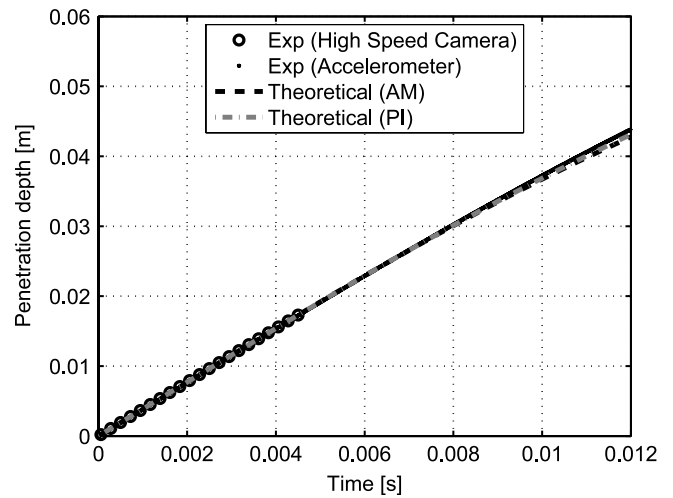
Fig. 20. Measured and calculated position on cone ($\beta = 20°$).

conservative, especially the added mass method. The height of the tested cone shape is 0.055 m, which means it is almost completely submerged after 12 ms (Fig. 20).

4.2.3. Cone 45°

Figs. 21–24 show the pressure distribution, acceleration, velocity and entry depth for the 45° cone with an impact velocity of 4.05 m/s. Although the classical Wagner principle assumes small deadrise angles, a quite good correspondence is found between theory and experiments for the first sensor position. However, the peak at the second sensor position seems to be significantly smaller than the first peak whereas the theory predicts the same values because of the similarity of the problem. The discrepancy between the two sensor positions has been observed for all impact velocities and is on average 35%. This pressure drop cannot be explained by a smaller instantaneous velocity, since the velocity during the second peak is about the same value as during the first peak. However, the accelerometer measures a small acceleration (during the first 10 ms) followed by a deceleration. The influence of this acceleration and deceleration 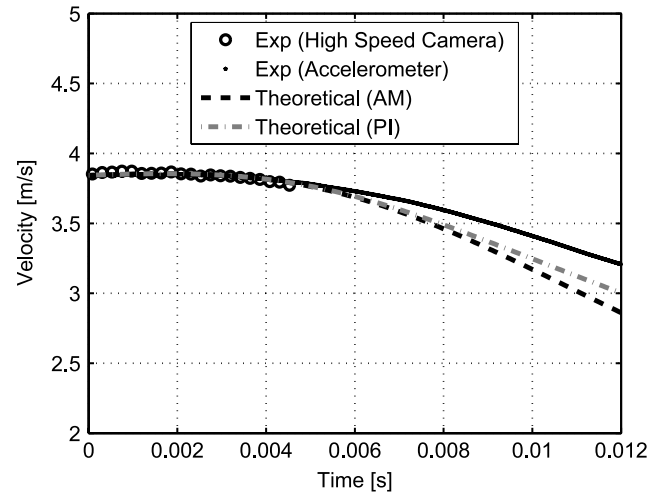on the pressure is not taken into account by the asymptotic theory. Assuming a uniform pressure distribution originating from the part of the impact force proportional to the acceleration ($M_{a_{33}} \frac{d^2 z}{dt^2}$), it is estimated that this contribution to the pressure is between 5% and 15% of the measured pressure, which is rather small and does not explain the pressure drop. A small time shift of 0.5 ms is observed between the pressure signals of sensor K30 and K31. As this corresponds to a vertical distance of 2.0 mm, which is a fraction of the sensor diameter of 5.5 mm, this shift might be caused by imperfections in the sensor mounting.

The deceleration, velocity and penetration are well predicted by the analytical approaches for small entry depths, since the pressures correspond well with the experiments in this case. The deceleration peak is -25 m/s^2, which is only one quarter of the peak measured for the cone 20°.

For this range of impact velocities the theoretical assumption of a constant impact velocity is acceptable for the 45° cone and the hemisphere. The 20° cone experiences the largest velocity drop, which is still smaller than 20% after almost complete submergence.

4.3. Comparison between shapes

Fig. 25–26 show the slamming pressure coefficient as a function of the dimensionless entry depth $U_0 t/R$ at $r/R = 0.267$,
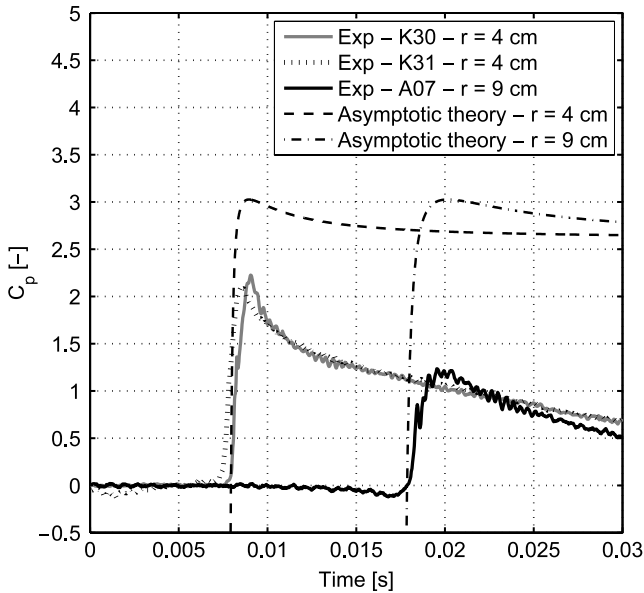
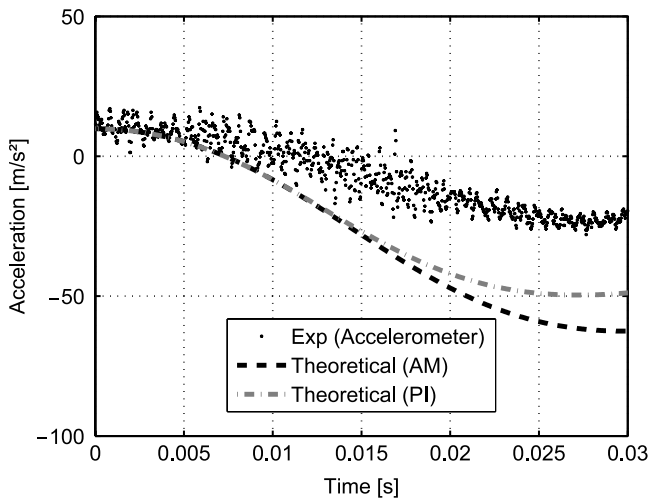**Fig. 21.** Measured and calculated pressure distribution on cone ($\beta = 45°$) for $V_0 = 4.05$ m/s.

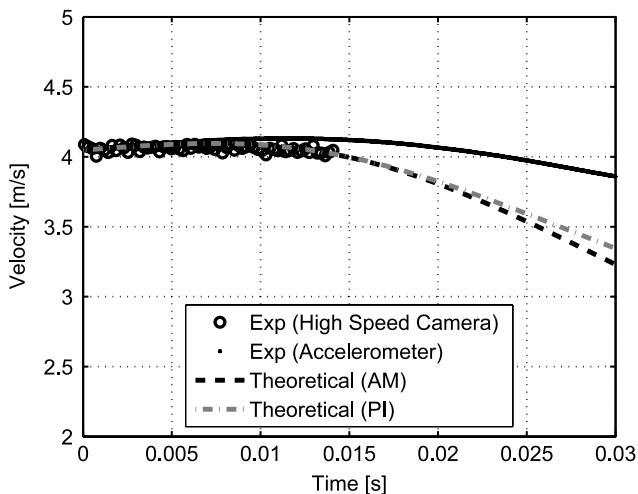**Fig. 22.** Measured and calculated acceleration on cone ($\beta = 45°$).

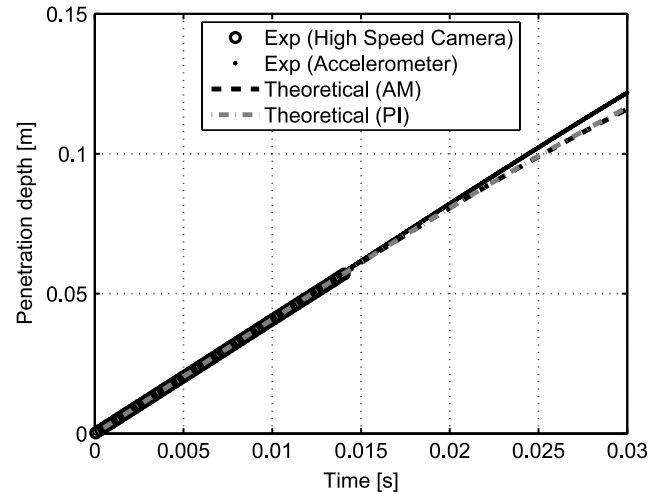**Fig. 23.** Measured and calculated velocity on cone ($\beta = 45°$).

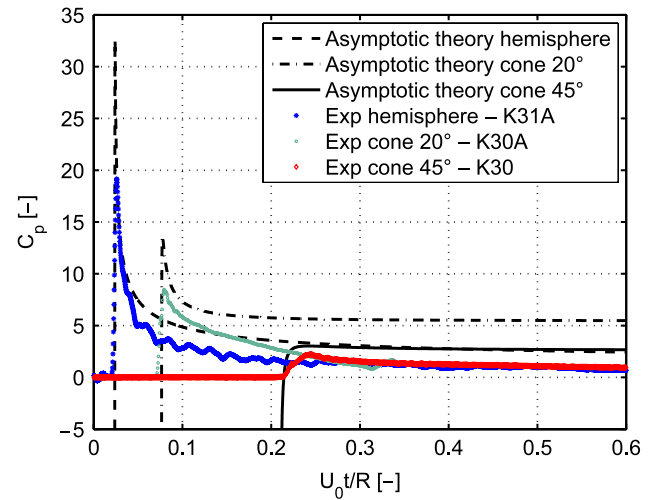**Fig. 24.** Measured and calculated position on cone ($\beta = 45°$).

Fig. 25. Slamming pressure coefficient at $r/R = 0.267$.

respectively $r/R = 0.300$. Although, the analytical solution is quite conservative in predicting the peak levels, the global pressure distribution fits the experiments quite well. In the bottom area, the hemisphere is subject to much higher slamming coefficients than the cones. For very small r-values, the local deadrise angle of the hemisphere tends to zero and very high impact pressures may occur. Material designers should pay special attention to this zone. For larger values of r/R the slamming coefficient on the hemisphere drops rapidly, which is not the case for the cones. Note in Fig. 26 that the peak value of the hemisphere is smaller than for the 20° cone, whereas the local deadrise angle of the former is only 18.4°.

4.4. Peak pressure

Material designers are often interested in maximum pressures. Figs. 27–30 give the maximum pressures as a function of the equivalent drop height, h^*, which corresponds to the drop height calculated from the measured impact velocity. The use of this equivalent drop height makes it possible to compare the measurement results with other research results. Since the maximum pressure is proportional to the drop height, a linear least squares fitting (LSF) has been adopted. The value of the squared Pearson correlation coefficient, R^2_*, is always very close to one, indicating a high linear correlation between the different data points of each test
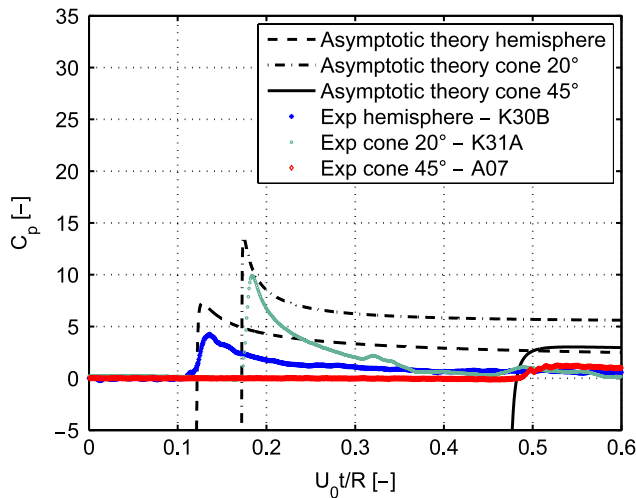
Fig. 26. Slamming pressure coefficient at $r/R = 0.300$.

Table 4
Coefficient of variation for the hemisphere and cone 20°, drop height = 1 m.

Coefficient of variation	A07 (%)	K30 (%)	K31 (%)
Hemisphere	0.66	8.48	0.44
Cone 20	0.93	12.22	1.25

series. The average deviation between the measured and analytical peak pressure levels can be easily assessed from the graphs. For the hemisphere, the measured peak values are respectively 58% and 55% of the Wagner peak values, for the first and second sensor position. For the 20° cone the ratios are 66% and 68% respectively and for the 45° cone 73% and 48%. The ratio between Chuang's experiments [27] and asymptotic theory is 27% and 86% for a cone with deadrise angle 3° and 15°, respectively. In [24] a numerical solution of the Wagner three-dimensional problem is suggested and evaluated by experiments on cone shapes with deadrise angles 6°, 10° and 14°. The ratios between the experiments and numerical solution are on average 53%, 67% and 76%, respectively and consequently comparable to the ratios found in this paper. Nisewanger [26] found pressure peaks on hemispheres that are closer to the asymptotic theory levels using pressure transducers with a diaphragm of 6.4 mm. Generally the blunt body approach is found to be conservative. This is considered as the main reason for the discrepancies between experiments and theory. Minor differences are attributed to the cell membrane diameter, which should be as small as possible. The assumption of a constant entry velocity might also have a small influence, depending on the shape and mass of the body. Furthermore the theory assumes rigid bodies, a condition which is seldom fulfilled in practice. Deformable bodies might experience significantly smaller pressure as demonstrated in [24].

In order to evaluate the reproducibility of the tests, the hemisphere and the 20° cone were each dropped ten times from a drop height of 1 m. The sensor positions correspond to the configurations in Fig. 3(b) and (d) for the hemisphere and cone, respectively. Table 4 shows the coefficient of variation C_v – the ratio of the standard deviation to the mean – of the measured peak pressures. For sensor A07 and K31 the relative spreading of the peak levels to the mean is extremely small. This indicates that these sensors measure very accurately and the tests are well reproducible. The larger spreading found for sensor K30 should be attributed to inaccuracies of the sensor itself.
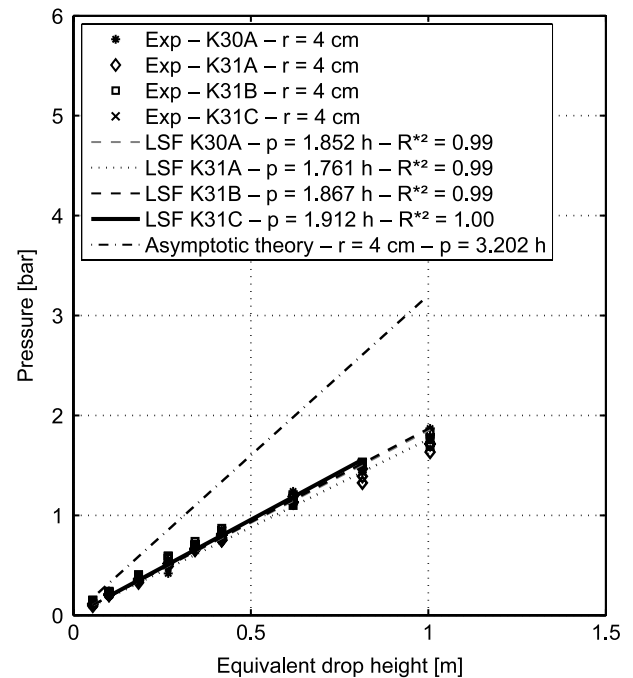

Fig. 27. Peak pressure as a function of drop height on hemisphere at $r = 0.04$ m.
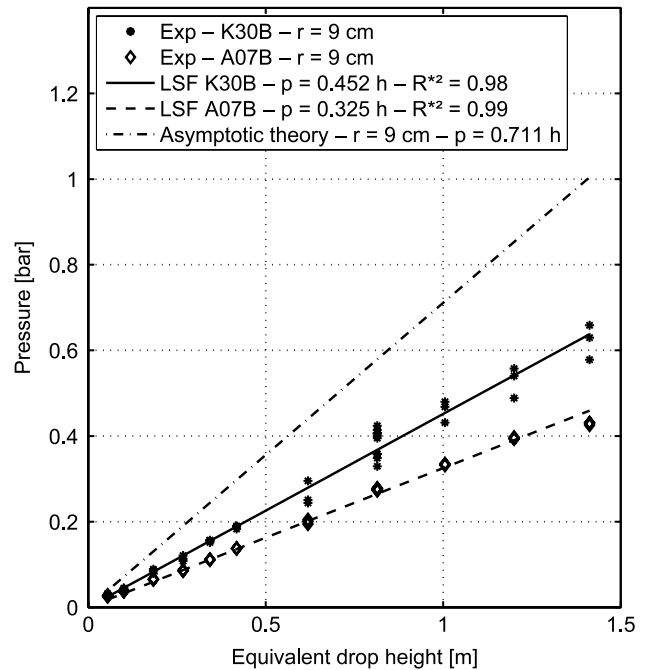

Fig. 28. Peak pressure as a function of drop height on hemisphere at $r = 0.09$ m.

5. Conclusion

Slamming phenomena on axisymmetric bodies have been experimentally studied by means of drop tests. A hemisphere and two cone shapes with deadrise angle 20° and 45° are dropped onto initially calm water. The water surface elevation is visualized with a high speed camera. Along the hemisphere the water uprise quickly ends in a spray, whereas a jet is attached to the body of the cone shapes. The wetting factor is determined for the cones and is about one fifth smaller than the value predicted by matching the outer three-dimensional flow with Wagner's two-dimensional jet flow model as described by Faltinsen in [7]. The
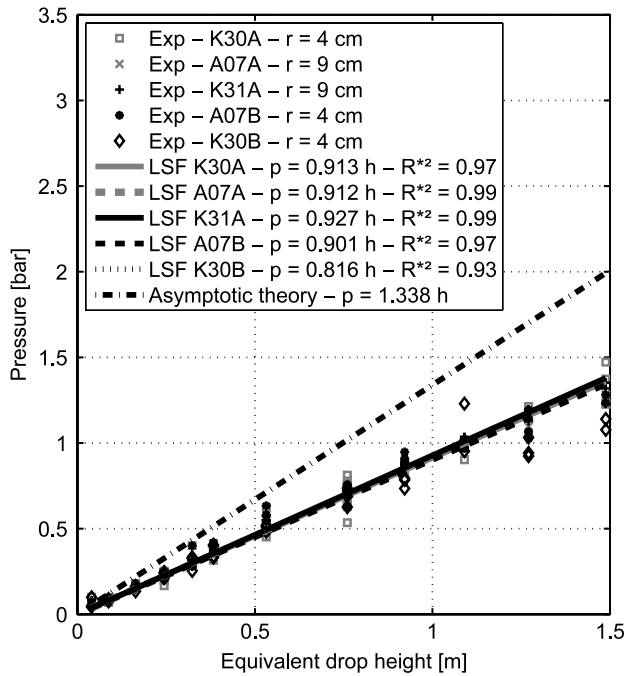
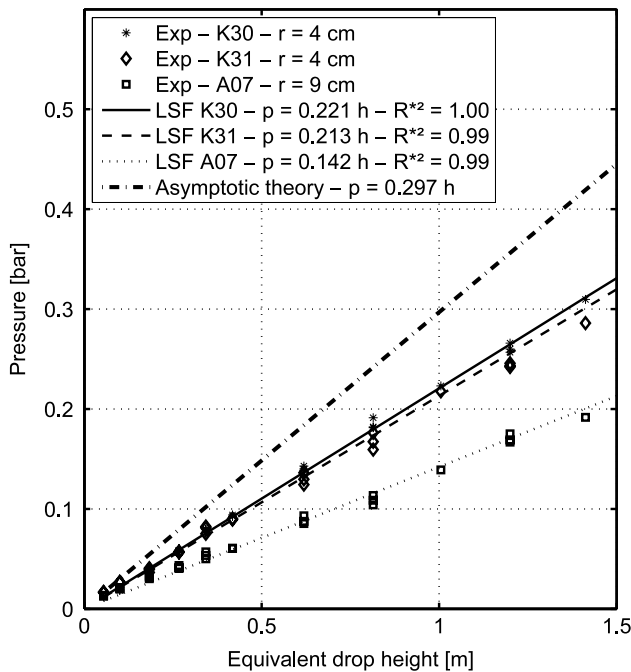**Fig. 29.** Peak pressure as a function of drop height on cone ($\beta = 20°$).

Fig. 30. Peak pressure as a function of drop height on cone ($\beta = 45°$).

pressure time history, impact velocity and deceleration are measured during impact. The velocity decrease during impact is found to be rather small, particularly for the 45° cone. In fact, for small entry velocities the 45° cone first experiences a very small velocity increase after making contact with the water surface. The measurements are compared with asymptotic theory for rigid axisymmetric bodies with constant entry velocity. Axisymmetric theory gives a good first idea of the slamming pressure distributions, however, it is found to be quite conservative. The ratio between measured and theoretical peak levels is roughly between 1/2 and 3/4, which is in

accordance with the findings of Peseux et al. [24] on cone shapes with smaller deadrise angles. To achieve better theoretical predictions, more advanced models should be applied in which e.g. the real body boundary conditions are satisfied, the variation of impact velocity is accounted for and possibly also the deformation of the body. Free fall outdoor drop tests with composite point absorbers at large scale have been performed very recently. The pressure profiles and deceleration are measured as well as the deformation of the structure during impact by means of strain gauges. These tests are a sequel to the previously described experiments and are intended to gain knowledge on the impact pressures and loads on flexible, large scale point absorber structures.

Acknowledgements

References

[1] Taghipour R, Arswendy A, Devergez M, Moan T. Efficient frequency-domain analysis of dynamic response for the multi-body wave energy converter in multi-directional waves. In: The 18th international offshore and polar engineering conference. 2008.

[2] Bjerrum A. The wave star energy concept. In: 2nd international conference on ocean energy. 2008.

[3] Falnes J. Ocean waves and oscillating systems, linear interactions including wave-energy extraction. Cambridge University Press; 2002.

[4] De Backer G, Vantorre M, Banasiak R, Beels C, De Rouck J. Numerical modelling of wave energy absorption by a floating point absorber system. In: 17th international offshore and polar engineering conference. 2007.

[5] De Backer G, Vantorre M, Victor S, De Rouck J, Beels C. Investigation of vertical slamming on point absorbers. In: 27th international conference on offshore mechanics and arctic engineering. 2008.

[6] Chuang S. Theoretical investigations on slamming of cone-shaped bodies. Journal of Ship Research 1969;13:276–83.

[7] Faltinsen O, Zhao R. Water entry of ship sections and axisymmetric bodies. In: AGARD FDP and Ukraine institute of hydromechanics workshop on highSpeed body motion in water. 1971.

[8] von Karman T. The impact of seaplane floats during landing, national advisory committee for aeronautics. Technical report 321. National Advisory Committee for Aeronautics. 1929.

[9] Wagner H. über stoss- und gleitvorgänge an der oberfläche von flüssigkeiten. Zeitschrift fur Angewandte Mathematik Und Mechanik 1932;12:193–215.

[10] Malleron N, Scolan Y-M, Korbkin A. Some aspects of a generalized wagner model. In: 22nd IWWWFB. Plitvice (Croatia). 2007. p. 137–40.

[11] Dobrovol'skaya Z. On some problems of similarity flow of fluid with a free surface. Journal of Fluid Mechanics 1969;36(4):805–25.

[12] Zhao R, Faltinsen O. Water entry of two-dimensional bodies. Journal of Fluid Mechanics 1993;246:593–612.

[13] Zhao R, Faltinsen O, Aarsnes J. Water entry of arbitrary two-dimensional sections with and without flow separation. In: ONR. Norway; 1996. p. 408–23.

[14] Mei X, Liu Y, Yue D. On the water impact of general two-dimensional sections. Applied Ocean Research 1999;21(1):1–15.

[15] Lin M-C, Shieh L-D. Flow visualization and pressure characteristics of a cylinder for water impact. Applied Ocean Research 1997;19(2):101–12.

[16] Yettou E-M, A. AD, Champoux Y. Experimental study on the water impact of a symmetrical wedge. Fluid Dynamics Research 2006;38(1):47–66.

[17] Shiffman M, Spencer D. The force of impact on a sphere striking a water surface. Appl. Math. Panel Rep. 42 IR AMG-NYU No. 105. 1945.

[18] Shiffman M, Spencer D. The force of impact on a cone striking a water surface. Communications on Pure and Applied Mathematics 1951;4:379–417.

[19] Miloh T. Wave slam on a sphere penetrating a free surface. Journal of Engineering Mathematics 1981;15(3):221–40.

[20] Miloh T. On the oblique water-entry problem of a rigid sphere. Journal of Engineering Mathematics 1991;25(1):77–92.

[21] Miloh T. On the initial-stage slamming of a rigid sphere in a vertical water entry. Applied Ocean Research 1991;13(1):34–48.

[22] Battistin D, Iafrati A. Hydrodynamic loads during water entry of two-dimensional and axisymmetric bodies. Journal of Fluids and Structures 2003; 17(5):643–64.

[23] Faltinsen O, Chezhian M. A generalized wagner method for three-dimensional slamming. Journal of Ship Research 2005;24(4):279–87.

[24] Peseux B, Gornet L, Donguy B. Hydrodynamic impact : Numerical and experimental investigations. Journal of Fluids and Structures 2005;21(3): 277–303.

[25] Kim Y, Hong S. Theoretical and numerical studies on three-dimensional water entry. In: 27th symposium on naval hydrodynamics. 2008.

[26] Nisewanger C. Experimental determination of pressure distribution on a sphere during water entry. Technical report 7808. NAVWEPS; 1961.

[27] Chuang S, Milne D. Drop tests of cones to investigate the three-dimensional effects of slamming. Technical report 3543. NSDRDC; 1971.

[28] Greenhow M, Lin W-M. Nonlinear free surface effects: Experiments and theory. Technical report 83–19. MIT; 1983.

[29] Greenhow M. Water-entry and -exit of a horizontal circular cylinder. Applied Ocean Research 1988;10(4):191–8.